Biomaterials 208 (2019) 72–82

Contents lists available at ScienceDirect

Biomaterials

journal homepage: www.elsevier.com/locate/biomaterials

Highly photostable two-photon NIR AIEgens with tunable organelle specificity and deep tissue penetration

Guangle Niu[a,b], Ruoyao Zhang[b,c], Yuan Gu[b], Jianguo Wang[b], Chao Ma[d], Ryan T.K. Kwok[a,b], Jacky W.Y. Lam[a,b], Herman H.-Y. Sung[b], Ian D. Williams[b], Kam Sing Wong[d], Xiaoqiang Yu[c], Ben Zhong Tang[a,b,e,*]

[a] HKUST-Shenzhen Research Institute, No. 9 Yuexing 1st RD, South Area, Hi-tech Park, Nanshan, Shenzhen, 518057, China
[b] Department of Chemistry, Hong Kong Branch of Chinese National Engineering Research Center for Tissue Restoration and Reconstruction, Institute for Advanced Study, Institute of Molecular Functional Materials, And Department of Chemical and Biological Engineering, The Hong Kong University of Science and Technology, Clear Water Bay, Kowloon, 999077, China
[c] Center of Bio and Micro/Nano Functional Materials, State Key Laboratory of Crystal Materials, Shandong University, Jinan, 250100, China
[d] Department of Physics, The Hong Kong University of Science and Technology, Clear Water Bay, Kowloon, 999077, China
[e] Center for Aggregation-Induced Emission, SCUT-HKUST Joint Research Institute, State Key Laboratory of Luminescent Materials and Devices, South China University of Technology, Guangzhou, 510640, China

ARTICLE INFO

Keywords:
High photostability
Two-photon
Near-infarared
AIEgen
Deep tissue penetration

ABSTRACT

Photostability is a particularly important parameter for fluorescence imaging especially long-term dynamic tracking in live samples. However, many organic fluorophores show poor photostability under one-photon and two-photon continuous irradiation. In addition, these traditional fluorophores also suffer from aggregation-caused quenching (ACQ) in aggregate state in insolvable water environment. Therefore, it remains challenging to develop photostable and ACQ-free fluorophores for biological imaging. In this work, we developed two highly photostable aggregation-induced emission luminogens (AIEgens) based on the cyanostilbene core for *in vitro* and *ex vivo* bioimaging. These AIEgens named CS-Py$^+$SO$_3^-$ and CS-Py$^+$ exhibit near-infrared solid-state emission, large Stokes shift (> 180 nm), high fluorescence quantum yield (12.8%–13.7%) and good two-photon absorption cross section (up to 88 GM). CS-Py$^+$SO$_3^-$ and CS-Py$^+$ show specific organelle staining with high biocompatibility in membrane and mitochondria in live cells, respectively. In addition, selective two-photon mitochondria visualization in live rat skeletal muscle tissues with deep-tissue penetration (about 100 μm) is successfully realized by using CS-Py$^+$. Furthermore, these AIEgens especially CS-Py$^+$ exhibit remarkably high resistance to photobleaching under one-photon and two-photon continuous irradiation. These highly photostable AIEgens could be potentially utilized in visualizing and tracking specific organelle-associated dynamic changes in live systems.

1. Introduction

Fluorescence imaging has received considerate attention in real-time tracking [1–4], visualization of dynamic change [5–8] and imaging-guided therapy [9–14] in live samples, due to its remarkable sensitivity, high selectivity, fast acquisition and easy operation [15–18]. The performance of fluorescence imaging is highly dependent on the fluorophore used. As a particularly important parameter of the fluorophore, photostability is usually under careful consideration for long-term tracking the dynamic change of biological events [19–21]. However, photostability is a common concern for traditional fluorophores especially commercial dyes like MitoTracker Green FM [22]. Such drawback of the fluorophores would inevitably bring some difficult capturing the optimal fluorescence image, resulting in waste of time and false biological signal. In addition, some photooxidation products resulting from photobleaching could also cause severe damage to live samples. The reason for the unstable resistance to photobleaching is generally caused by the small amount of these traditional fluorophores used. However, increase the concentration of fluorophores often suffer from aggregation-caused quenching (ACQ) [22]. Therefore, development of novel fluorophores with enhanced photostability as well as inhibited ACQ effect is of particular importance.

Our group discovered the unique feature that organic fluorophores show no or faint emission in organic solvent but highly boosted

* Corresponding author. HKUST-Shenzhen Research Institute, No. 9 Yuexing 1st RD, South Area, Hi-tech Park, Nanshan, Shenzhen, 518057, China.
E-mail address: tangbenz@ust.hk (B.Z. Tang).

https://doi.org/10.1016/j.biomaterials.2019.04.002
Received 19 February 2019; Received in revised form 3 April 2019; Accepted 4 April 2019
Available online 09 April 2019
0142-9612/

emission in aggregate or solid state, and this phenomenon was first termed as aggregation-induced emission (AIE) [23]. A new concept restriction of intramolecular motion (RIM) was proposed to explain such unique phenomenon [22]. Based on RIM, aggregation-induced emission luminogens (AIEgens) are applied for biomedical imaging with increased concentration, leading to high photostability as well as bright emission [24–33]. Indeed, many of our AIEgens are successfully demonstrated to exhibit high resistance to photobleaching in biological imaging [34–42]. For example, our group recently in collaboration with Prof. Qian prepared AIEgen doped colloidal mesoporous silica nanoparticles for super-resolution imaging with high resistance to photobleaching even under long-term and high-power stimulated emission depletion light irradiation [43]. Thus, highly photostable AIEgens are becoming promising and first-choice tools for fluorescence imaging.

Compared with short-wavelength emissive fluorophores, long-wavelength emissive especially near-infrared (NIR) AIEgens hold tremendous advantages for bioimaging because of deep tissue penetration, minimal photodamage and high signal-to-noise ratio in live biological samples [44,45]. Generally, extending the π-conjugation of the skeleton of AIEgens is an effective method to construct NIR AIEgens [22]. However, with increased π-conjugation, the cell penetration of such AIEgens generally significantly decreases. Construction of donor-π-acceptor (D-π-A) structure is another effective method to develop NIR AIEgens, but the twisted intramolecular charge transfer (TICT) effect should be carefully under consideration. Because strong TICT effect sometimes could result in AIEgens with very low fluorescence quantum yield [46]. Indeed, most of NIR AIEgens are synthesized by adopting these two strategies simultaneously. So far, the majority of NIR AIEgens are fabricated organic nanoparticles (NPs) by using amphiphilic surfactants to realize their internalization in live samples [47,48]. However, it's complicated and time-consuming to fabricate these NIR AIEgen NPs, and the commercial amphiphilic surfactants used like DSPE-PEG are very expensive. Therefore, it remains challenging to develop inherent NIR AIEgens with excellent penetrability in live cells and tissues.

Cyanostilbenes [49], a family of D-π-A based AIEgens, have been extensively investigated and applied in many fields such as self-assembly, chemosensor and bioimaging, due to their facile synthesis and easy purification [50–52]. Previous studies have demonstrated that introduction of strong electron withdrawing groups like -F and -CN can improve the fluorophores' resistance to photobleaching [53,54]. Based on this strategy, we anticipated that slightly modified cyanostilbenes could probably become inherent photostable AIEgens. In addition, further introduction of electron withdrawing group like pyridinium into the skeleton of D-π-A based cyanostilbenes can enhance the TICT effect, probably resulting in narrow energy gap and NIR emissive AIEgens [55–57]. Though some achievements have been made to develop NIR cyanostilbenes, these AIEgens basically showed very low cell penetrability and NPs were fabricated to demonstrate their application in bioimaging [58,59]. On the other hand, eukaryotic cells contain numerous membrane-enclosed organelles (cell membrane, mitochondria and Golgi apparatus et al.). Long alkyl chain modified AIEgens with different electrical charge distributions probably showed strong interaction with the main component of membrane amphipathic phospholipid, leading to increased penetrability and location in specific organelles [60–63]. Thus the balance between hydrophobicity and electrical charge distributions should be carefully adjusted.

Take the above-mentioned issues together, cyanostilbene with a long alkyl chain substituent was adopted as the AIEgen core and D-π-A structure was further introduced in the cyanostilbene skeleton to red shift the fluorescence as well as enhance the TICT effect. In addition, these AIEgens endowed with different charge distributions were explored to investigate the specific location in live samples. In the present work, we indeed synthesized two photostable cyanostilbene based AIEgens (CS-Py$^+$SO$_3^-$ and CS-Py$^+$, Scheme 1) with a long alkyl chain substituent. These AIEgens exhibit solid-state NIR emission and obvious TICT effect due to strong D-π-A effect. CS-Py$^+$SO$_3^-$ and CS-Py$^+$ with different charge distributions show specific organelle staining with high biocompatibility in membrane and mitochondria in live cells, respectively. Furthermore, CS-Py$^+$ was applied for staining in live rat skeletal muscle tissues with deep-tissue penetration under two-photon excited imaging mode. To the best of our knowledge, this is the first time to explore the long alkyl chain substituted and NIR emissive cyanostilbene derivatives for *in vitro* and *ex vivo* bioimaging. Of particular interest is that these two AIEgens especially CS-Py$^+$ exhibit remarkable resistance to photobleaching under continuous irradiation with one-photon and two-photon lasers.

2. Experimental Section

2.1. Materials and methods

All chemicals were used as received without further purification unless otherwise specified. Anhydrous DMSO and THF were used for fluorescence property investigation. Deionized water was used throughout this study. Commercial membrane dye DiI and Mitochondria dye MitoTracker Deep Red FM (MTDR) were purchased from ThermoFisher Scientific. ^{1}H NMR (400 MHz), ^{13}C NMR (100 MHz) and ^{19}F NMR (376 MHz) spectra were recorded on a Bruker ARX 400 spectrometer using tetramethylsilane (TMS) as internal standard. High-resolution mass spectra (HRMS) were recorded on a GCT premier CAB048 mass spectrometer operated in a MALDI-TOF mode. UV–Vis absorption and fluorescence spectra were recorded with Milton Roy Spectronic 3000 Array spectrameter and PerkinElmer LS 55 Spectrofluometer, respectively. All the fluorescence quantum yields were determined using an integrating sphere. Two-photon excited fluorescence spectra in solution were measured on a Coherent Mira 900 and the pump laser beam (800–980 nm) came from a mode-locked Ti:sapphire laser system at the pulse duration of femtosecond pulses with a repetition rate of 76 MHz. Two-photon absorption cross sections have been measured by the two-photon excited fluorescence method with rhodamine B in methanol as the standard [57,64].

2.2. Cell culture and in vitro live cell imaging

HeLa cells were cultured in confocal dishes in the culture medium (Dulbeccos modified Eagle medium (DMEM), supplemented with 10% fetal bovine serum (FBS) and 1% penicillin and streptomycin) in 5% CO_2/air at 37 °C in a humidified incubator for 24 h. Fresh DMEM medium containing 1 μM CS-Py$^+$SO$_3^-$ and CS-Py$^+$ (Stocked solution in DMSO, 1 mM) was added into the culture medium of HeLa cells and incubated at 37 °C in 5% CO_2 for 15 min before the imaging. For co-stain imaging, HeLa cells were treated and incubated with 0.2 μM DiI or MitoTraker Deep Red FM (MTDR). Cells were washed with phosphate-buffered saline (PBS, pH = 7.4). Confocal fluorescence imaging data were obtained with an Olympus FV 1200 or Zeiss LSM 800 Confocal Laser Scanning Microscope (For CS-Py$^+$SO$_3^-$ and CS-Py$^+$, excitation 488 nm, emission collection 520–620 nm; For DiI, excitation 543 nm, emission collection 580–680 nm; For MTDR, excitation 635 nm, emission collection 650–750 nm). For one-photon photostability test, cells incubated with different dyes were continuously irradiated with confocal lasers (For CS-Py$^+$SO$_3^-$ and CS-Py$^+$, 488 nm laser, laser power of 12%; for DiI, 543 nm laser, laser power 12%; for MTDR, 635 nm laser, laser power 12%). The image was scanned about every 2.1 s.

2.3. Ex vivo imaging in live rat skeletal muscle tissues

The rat skeletal muscle tissues were directly removed from just killed adult wistar rat. The tissues were stained with CS-Py$^+$ (1 μM) at room temperature in culture medium (DMEM, supplemented with 10% FBS and 1% penicillin and streptomycin) in 5% CO_2/air at 37 °C in a humidified incubator for 1 h. The tissues were washed with phosphate-

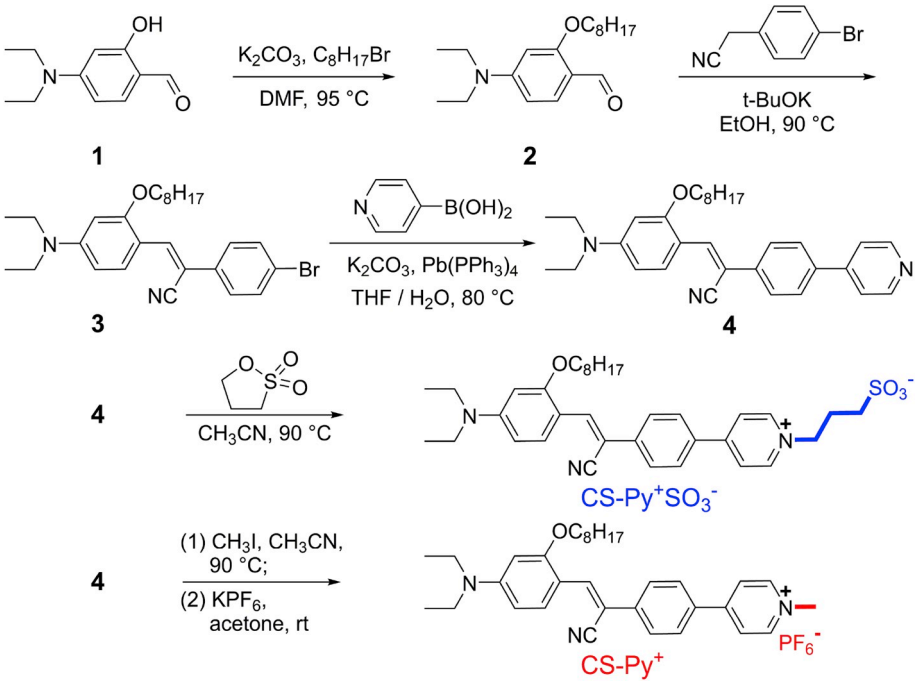

Scheme 1. Synthesis routes to CS-Py$^+$SO$_3^-$ and CS-Py$^+$.

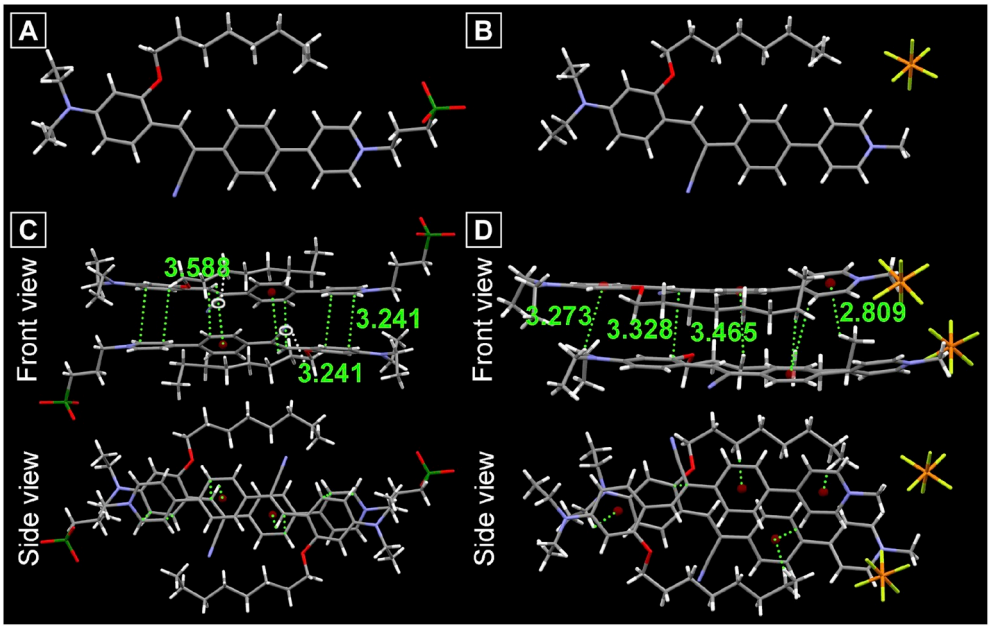

Fig. 1. Single crystal structures of (A) CS-Py$^+$SO$_3^-$ and (B) CS-Py$^+$. C, gray; N, blue; O, red; F, yellow; S, green; P, orange. Molecular packing in the crystal of (C) CS-Py$^+$SO$_3^-$ and (D) CS-Py$^+$. Distances in Å. (For interpretation of the references to colour in this figure legend, the reader is referred to the Web version of this article.)

buffered saline (PBS, pH = 7.4) before two-photon imaging. Two-photon fluorescent images were collected using a stimulated emission depletion microscopy (Leica Stimulated Emission Depletion Microscope) equipped with a multiphoton laser (Coherent Chameleon Ultra II Multiphoton laser). The excitation wavelength was 900 nm from a Ti:sapphire femtosecond laser source and the two-photon excited fluorescence was collected from 520 to 620 nm. For two-photon photostability test, live tissues incubated with CS-Py$^+$ were continuously irradiated with 900-nm pulsed laser (output intensity of 2476 mW), and the image was scanned about every 5.2 s. These experiments were performed in compliance with the relevant laws and institutional guidelines. The institutional committee had approved the experiments.

2.4. Synthesis of compound 2

Compound 1 (1.93 g, 10 mmol), K_2CO_3 (1.52 g, 11 mmol) and $C_8H_{17}Br$ (2.11 g, 11 mmol) were successively added to the anhydrous DMF (20 mL) in a round bottomed flask, and the mixture was stirred at 95 °C for 6 h. After cooling to room temperature, the solvent was removed under reduced pressure, and the residue was purified by silica gel chromatography using Hexane/AcOEt (from 2:1, 1:1 to 1:2, *v/v*) as the eluent to give compound **2** as a yellow oily liquid (2.84 g, 93%). ^{1}H NMR (400 MHz, $CDCl_3$): δ 10.18 (s, 1H), 7.71 (d, J = 9.0 Hz, 1H), 6.27 (dd, J_1 = 8.9 Hz, J_2 = 1.9 Hz, 1H), 6.01 (d, J = 2.3 Hz, 1H), 4.02 (t, J = 6.4 Hz, 2H), 3.42 (q, J = 7.1 Hz, 4H), 1.88–1.78 (m, 2H), 1.53–1.43 (m, 2H), 1.40–1.25 (m, 8H), 1.21 (t, J = 7.1 Hz, 6H), 0.89 (t,

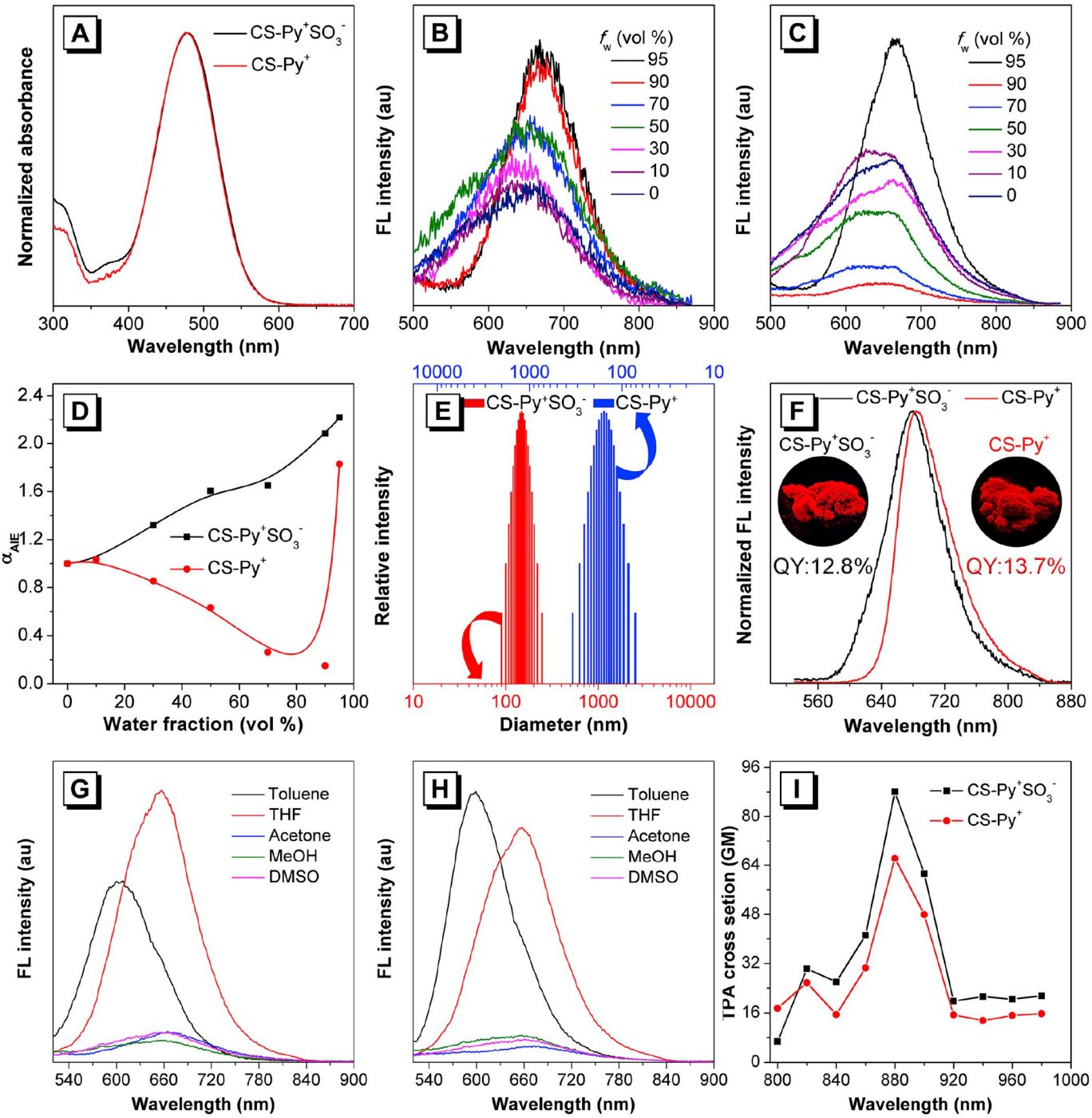

Fig. 2. (A) Normalized absorption spectra of CS-Py$^+$SO$_3^-$ (5 μM) and CS-Py$^+$ (5 μM) in DMSO. Fluorescence spectra of (B) CS-Py$^+$SO$_3^-$ (5 μM) and (C) CS-Py$^+$ (5 μM) in DMSO and DMSO/water mixture with different water fractions. (D) Plots of α_{AIE} (fluorescence intensity I/I_0) versus the composition of the DMSO/water mixtures of CS-Py$^+$SO$_3^-$ and CS-Py$^+$. (E) Dynamic light scattering data of CS-Py$^+$SO$_3^-$ and CS-Py$^+$ in water containing 5% DMSO. (F) Normalized fluorescence spectra of CS-Py$^+$SO$_3^-$ and CS-Py$^+$ in solid state. Inset: Fluorescent photos of solids of CS-Py$^+$SO$_3^-$ and CS-Py$^+$ taken under 365 nm UV irradiation from a handheld UV lamp. Fluorescence spectra of (G) CS-Py$^+$SO$_3^-$ and (H) CS-Py$^+$ in different polar solvents. (I) Two-photon absorption (TPA) cross sections of CS-Py$^+$SO$_3^-$ and CS-Py$^+$ in THF. 1 GM = 10^{-50} cm^4 s/photon.

J = 6.9 Hz, 3H). ^{13}C NMR (100 MHz, $CDCl_3$): δ 187.21, 163.98, 153.92, 130.12, 114.36, 104.27, 93.23, 68.12, 44.82, 31.86, 29.40, 29.29, 29.22, 26.20, 22.71, 14.15, 12.67. HRMS (MALDI-TOF): m/z calcd for $[C_{19}H_{32}NO_2]^+$ 306.2428 ($[M+H]^+$), found 306.2437.

2.5. Synthesis of compound 3

4-Bromophenylacetonitrile (388 mg, 2 mmol) and t-BuOK (224 mg, 2 mmol) were successively added to the anhydrous EtOH (20 mL) in a round bottomed flask, which was stirred at room temperature for 10 min. Then compound **2** (610 mg, 2 mmol) was added to the solution, and the mixture was refluxed at 90 °C for 6 h. After cooling to room temperature, the solvent was removed under reduced pressure, and the residue was purified by silica gel chromatography using Hexane/AcOEt (3:1, v/v) as the eluent to give compound **3** as a yellow solid (712 mg, 74%). ^{1}H NMR (400 MHz, $CDCl_3$): δ 8.28 (d, J = 9.0 Hz, 1H), 7.95 (s,

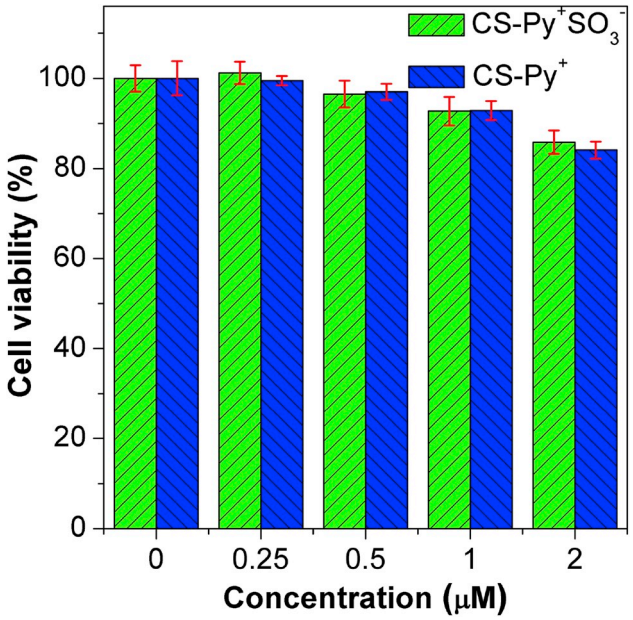

Fig. 3. The cytotoxicity of CS-Py$^+$SO$_3^-$ and CS-Py$^+$ in HeLa cells.

1H), 7.53–7.45 (m, 4H), 6.35 (dd, J_1 = 9.0 Hz, J_2 = 2.4 Hz, 1H), 6.09 (d, J = 2.4 Hz, 1H), 4.00 (t, J = 6.4 Hz, 2H), 3.42 (q, J = 7.1 Hz, 4H), 1.87–1.79 (m, 2H), 1.53–1.44 (m, 2H), 1.41–1.25 (m, 8H), 1.22 (t, J = 7.1 Hz, 6H), 0.88 (t, J = 6.9 Hz, 3H). ^{13}C NMR (100 MHz, $CDCl_3$): δ 159.95, 151.37, 137.13, 135.52, 131.97, 129.44, 126.93, 121.34, 119.88, 110.74, 104.49, 101.51, 94.36, 68.50, 44.79, 31.90, 29.49, 29.43, 29.35, 26.39, 22.80, 14.23, 12.84. HRMS (MALDI-TOF): m/z calcd for [$C_{27}H_{35}BrN_2O$] 482.1933 ([M]), found 482.1932.

2.6. Synthesis of compound **4**

A mixture of compound **3** (434 mg, 0.9 mmol), K_2CO_3 (138 mg, 1 mmol), $Pd(PPh_3)_4$ (15 mg, 0.013 mmol) and 4-pyridylboronic acid (123 mg, 1 mmol) in THF/H_2O (9 mL/1 mL) was refluxed at 80 °C for 12 h under nitrogen. After cooling to room temperature, the solvent was removed under reduced pressure, and the residue was purified by silica gel chromatography using Hexane/AcOEt (from 2:1 to 1:1, v/v) as the eluent to give compound **4** as an orange solid (338 mg, 78%). ^{1}H NMR (400 MHz, $CDCl_3$): δ 8.67 (dd, J_1 = 4.7 Hz, J_2 = 1.4 Hz, 2H), 8.33 (d, J = 9.0 Hz, 1H), 8.06 (s, 1H), 7.77–7.65 (m, 4H), 7.53 (dd, J_1 = 4.5 Hz, J_2 = 1.6 Hz, 2H), 6.37 (dd, J_1 = 9.1 Hz, J_2 = 2.4 Hz, 1H), 6.11 (d, J = 2.4 Hz, 1H), 4.02 (t, J = 6.4 Hz, 2H), 3.43 (q, J = 7.1 Hz, 4H), 1.90–1.81 (m, 2H), 1.56–1.46 (m, 2H), 1.43–1.26 (m, 8H), 1.23 (t, J = 7.1 Hz, 6H), 0.86 (t, J = 6.9 Hz, 3H). ^{13}C NMR (100 MHz, $CDCl_3$): δ 160.04, 151.43, 150.45, 147.59, 137.38, 137.25, 136.89, 129.53, 127.44, 126.01, 121.41, 120.01, 110.85, 104.54, 101.70, 94.36, 68.51, 44.80, 31.90, 29.49, 29.43, 29.36, 26.40, 22.80, 14.22, 12.85. HRMS (MALDI-TOF): m/z calcd for [$C_{32}H_{39}N_3O$] 481.3093 ([M]), found 481.3073.

2.7. Synthesis of CS-Py$^+$SO$_3^-$

A mixture of compound **4** (385 mg, 0.8 mmol) and 1,3-propanesultone (122 mg, 1 mmol) in CH_3CN (10 mL) was refluxed at 90 °C for 4 h. After cooling to room temperature, Et_2O (30 mL) was added to the solution. The solid was filtered off and purified by silica gel chromatography using CH_2Cl_2/MeOH (from 15:1, 10:1 to 6:1, v/v) as the eluent

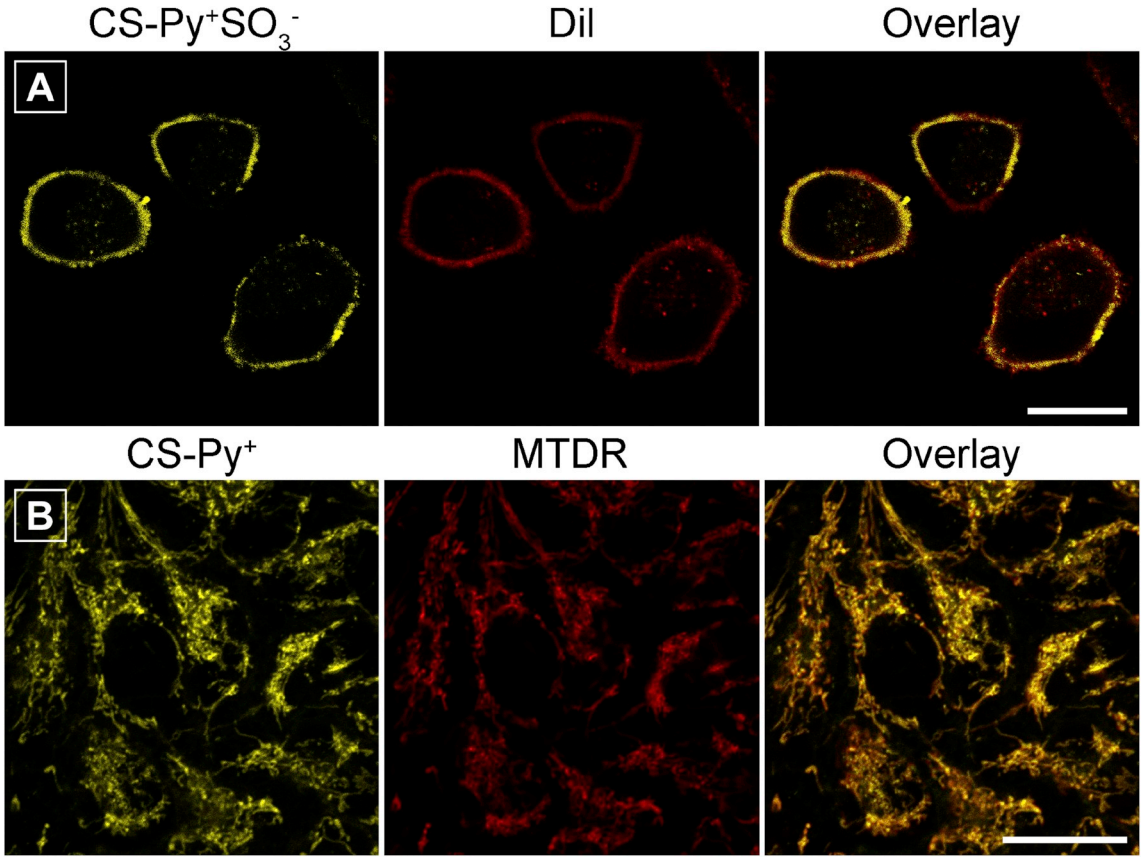

Fig. 4. *In vitro* one-photon imaging in live cells. Confocal laser scanning microscopy images of live HeLa cells incubated with (A) CS-Py$^+$SO$_3^-$ (1 μM) and DiI (0.2 μM) and (B) CS-Py$^+$ (1 μM) and MTDR (0.2 μM). Scale bar: 20 μm.

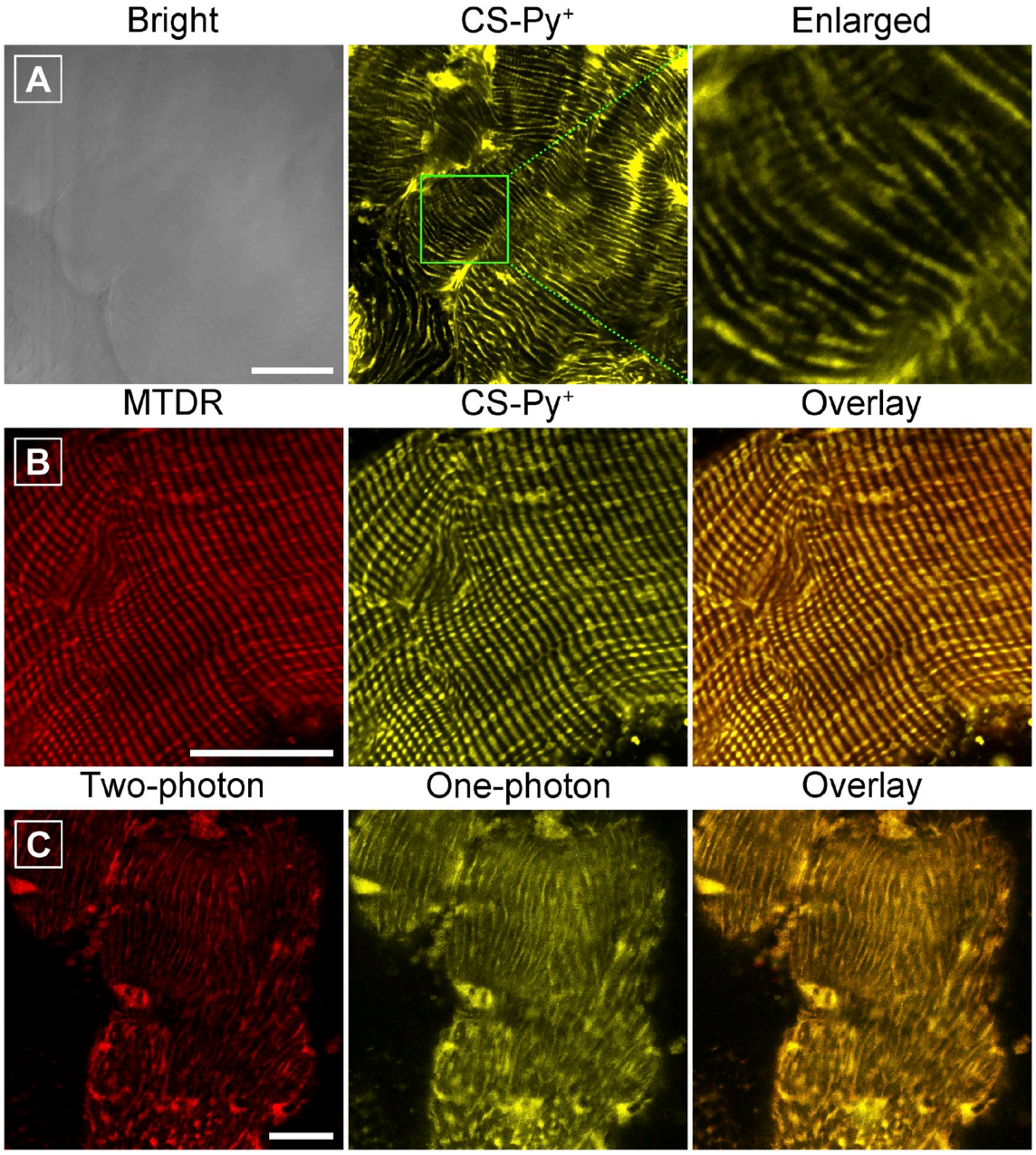

Fig. 5. *Ex vivo* one-photon and two-photon imaging in live tissues. One-photon fluorescent microscopic images of rat skeletal muscle tissues incubated (A) only with CS-Py$^+$ (1 μM) and (B) with CS-Py$^+$ (1 μM) and MTDR (0.5 μM). (C) One-photon (λ_{ex} = 488 nm) and two-photon (λ_{ex} = 900 nm) fluorescent microscopic images of rat skeletal muscle tissues incubated with CS-Py$^+$ (1 μM). Scale bar: 20 μm.

to give CS-Py$^+$SO$_3^-$ as a dark red solid (295 mg, 61%). ^{1}H NMR (400 MHz, DMSO-d_6): δ 9.09 (d, J = 6.9 Hz, 2H), 8.53 (d, J = 6.8 Hz, 2H), 8.22–8.08 (m, 4H), 7.78 (d, J = 8.5 Hz, 2H), 6.47 (dd, J_1 = 9.3 Hz, J_2 = 1.8 Hz, 1H), 6.23 (d, J = 1.7 Hz, 1H), 4.71 (t, J = 6.9 Hz, 2H), 4.10 (t, J = 6.2 Hz, 2H), 3.46 (q, J = 6.9 Hz, 4H), 2.46 (overlapped with DMSO-d_6, t, J = 7.2 Hz, 2H), 2.30–2.21 (m, 2H), 1.84–1.74 (m, 2H), 1.51–1.41 (m, 2H), 1.39–1.18 (m, 8H), 1.15 (t, J = 7.0 Hz, 6H), 0.78 (t, J = 6.7 Hz, 3H). ^{13}C NMR (100 MHz, $CDCl_3/CD_3OD$ = 2:1): δ 160.38, 155.71, 152.02, 144.50, 141.01, 138.74, 131.30, 129.47, 128.28, 126.09, 124.26, 119.54, 110.23, 104.54, 99.19, 93.89, 68.30, 58.87, 46.37, 44.62, 31.58, 29.12, 29.09, 28.97, 27.05, 26.02, 22.45, 13.76, 12.42. HRMS (MALDI-TOF): m/z calcd for $[C_{35}H_{46}N_3O_4S]^+$ 604.3204 ($[M+H]^+$), found 604.3220.

2.8. Synthesis of CS-Py$^+$

A mixture of compound **4** (385 mg, 0.8 mmol) and CH_3I (142 mg, 1 mmol) in CH_3CN (5 mL) was refluxed at 90 °C for 4 h. After cooling to room temperature, Et_2O (30 mL) was added to the solution. The solid was filtered off and dried under vacuum. The obtained solid was used in the next step without further purification. Then the obtained solid was dissolved in acetone (10 mL), and a solution of KPF_6 (915 mg, 5 mmol) in 2 mL H_2O was added. The mixture was stirred at room temperature for 24 h. Acetone was removed under reduced pressure, and the residue was purified by silica gel chromatography using CH_2Cl_2/MeOH (from 20:1, 15:1 to 10:1, *v/v*) as the eluent to give CS-Py$^+$ as a dark red-brown solid (298 mg, 58%). ^{1}H NMR (400 MHz, DMSO-d_6): δ 9.00 (d,

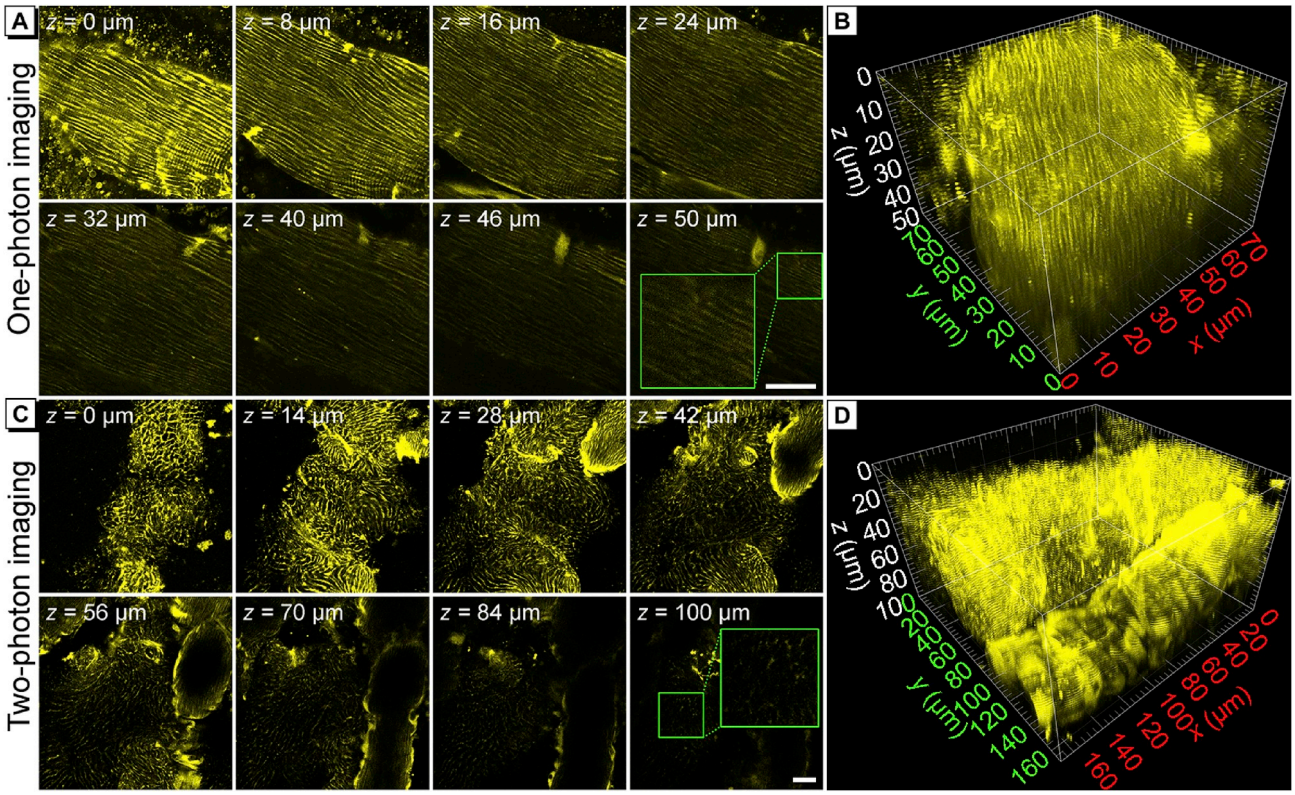

Fig. 6. *Ex vivo* one-photon and two-photon imaging in live deep tissues. (A) One-photon (λ_{ex} = 488 nm) and (C) two-photon (λ_{ex} = 900 nm) fluorescent microscopic images of the mouse skeletal muscle tissue stained with CS-Py$^+$ (1 μM) at different penetration depths along *z*-axis. Scale bar: 20 μm. Reconstructed 3D (B) one-photon and (D) two-photon fluorescent microscopic images.

J = 6.9 Hz, 2H), 8.52 (d, J = 7.0 Hz, 2H), 8.21–8.09 (m, 4H), 7.79 (d, J = 8.7 Hz, 2H), 6.47 (dd, J_1 = 9.2 Hz, J_2 = 2.2 Hz, 1H), 6.24 (d, J = 2.1 Hz, 1H), 4.32 (s, 3H), 4.10 (t, J = 6.4 Hz, 2H), 3.47 (q, J = 6.9 Hz, 4H), 1.84–1.75 (m, 2H), 1.51–1.42 (m, 2H), 1.40–1.18 (m, 8H), 1.15 (t, J = 7.0 Hz, 6H), 0.78 (t, J = 6.8 Hz, 3H). ^{13}C NMR (100 MHz, DMSO-d_6): δ 159.95, 153.14, 151.79, 145.58, 139.29, 137.91, 131.95, 128.87, 128.80, 125.45, 123.57, 119.35, 109.43, 104.52, 99.07, 94.33, 68.05, 47.01, 44.03, 31.15, 28.69, 28.47, 25.67, 22.07, 13.92, 12.57.^{19}F NMR (376 MHz, DMSO-d_6): δ −69.20 (s, 3F), −71.09 (s, 3F). HRMS (MALDI-TOF): m/z calcd for $[C_{33}H_{42}N_3O]^+$ 496.3322 ($[M]^+$), found 496.3337.

3. Results and discussion

3.1. Synthesis and characterization

The synthesis routes to cyanostilbene based AIEgens CS-Py$^+$SO$_3^-$ and CS-Py$^+$ are outlined in Scheme 1. Compound **2** was synthesized by alkylation of commercial compound **1** in the presence of $C_8H_{17}Br$ and K_2CO_3 in heated DMF. Then compound **2** reacted with 4-bromophenylacetonitrile in the presence of *t*-BuOK in refluxed anhydrous EtOH, resulting in compound **3**. Compound **4** could be obtained by Suzuki coupling reaction of compound **3** and 4-pyridinylboronic acid. Finally, reaction of compound **4** and 1,3-propanesultone resulted in CS-Py$^+$SO$_3^-$. Methylation and then anion exchange of compound **4** led to CS-Py$^+$. The structures of the inter-mediate compounds (**2**, **3** and **4**) and the final products (CS-Py$^+$SO$_3^-$ and CS-Py$^+$) were characterized by ^{1}H NMR, ^{13}C NMR, ^{19}F NMR and HRMS (Fig. S1eS13). The detailed synthetic procedures were shown in the Experimental Section.

The structures of CS-Py$^+$SO$_3^-$ and CS-Py$^+$ were further confirmed by X-ray crystal structure analysis (CCDC 1851671–1851672, Figs. 1 and S14). Single crystals of CS-Py$^+$SO$_3^-$ and CS-Py$^+$ suitable for X-ray structure analysis were obtained by slow evaporation of mixed solvent of CH_2Cl_2 and MeOH (CH_2Cl_2/MeOH = 2:1, *v/v*) at ambient temperature. The details of the X-ray experimental conditions, cell data, and refinement data of CS-Py$^+$SO$_3^-$ and CS-Py$^+$ are summarized in Table S1eS2. CS-Py$^+$SO$_3^-$ and CS-Py$^+$ exhibit intramolecular π-π interaction and C–H···π interaction (Fig. 1C and D). The molecules of CS-Py$^+$SO$_3^-$ in the crystal lattice are arranged in a head-to-tail antiparallel arrangement, resulting in strong intermolecular donor-acceptor interaction, while those of CS-Py$^+$ in the crystal lattice showed head-to-head arrangement. Multiple intramolecular interactions, such as C–H···O, C–H···N, C–H···π, C–H···F and P–F···π interactions, exist to stabilize these different packing modes of CS-Py$^+$SO$_3^-$ and CS-Py$^+$, which could benefit for the restriction of intramolecular motion (RIM) and blocking the non-radiative processes in the aggregated state.

3.2. Photophysical property

The absorption and fluorescence (FL) data of CS-Py$^+$SO$_3^-$ and CS-Py$^+$ were investigated, and corresponding spectra were shown in Fig. 2 and Fig. S15eS16 and the data were summarized in Table S3. AIEgen CS-Py$^+$SO$_3^-$ and CS-Py$^+$ exhibit very similar absorption (Fig. 2A), with absorption peaks (λ_{abs}) at 478 nm and 477 nm for CS-Py$^+$SO$_3^-$ and CS-Py$^+$, respectively. CS-Py$^+$SO$_3^-$ showed very low near-infrared (NIR) fluorescence (NIR emission peak λ_{em} of about 658 nm) in dilute DMSO, and with increased water fraction (f_w) in the DMSO/water mixtures, the emission intensity of CS-Py$^+$SO$_3^-$ showed slow increase while the wavelength peak showed very slight change (Fig. 2B). For CS-Py$^+$, it also showed typical aggregation-enhanced emission (AEE) property. The difference between CS-Py$^+$SO$_3^-$ and CS-Py$^+$ is that the aggregates (f_w = 95% in the DMSO/water mixture) of CS-Py$^+$ showed enhanced and blue-shifted emission (Fig. 2C), which probably results from twisted structure and intramolecular charge transfer (ICT) property. It should be noted that FL of CS-Py$^+$SO$_3^-$ and CS-Py$^+$ in high water fraction (f_w = 95%) increased only several-fold compared with

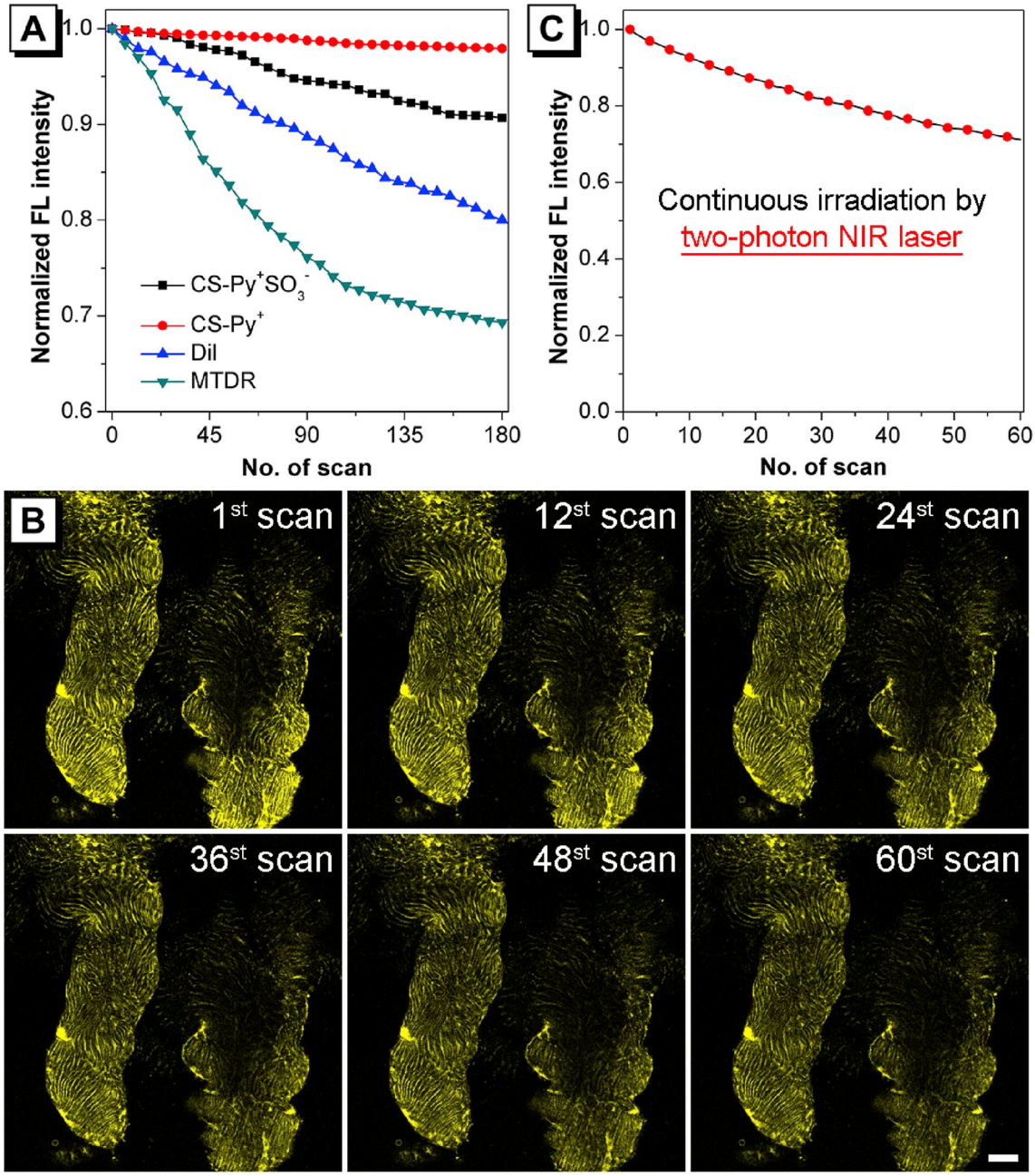

Fig. 7. (A) Normalized fluorescence intensity of CS-Py$^+$SO$_3^-$, CS-Py$^+$, DiI and MTDR in HeLa cells by continuous irradiation with confocal lasers. Irradiation conditions: for CS-Py$^+$SO$_3^-$ and CS-Py$^+$, 488 nm laser, laser power 12%; for DiI, 543 nm laser, laser power 12%; for MTDR, 635 nm laser, laser power 12%. The image was scanned about every 2.1 s. (B) Two-photon fluorescent images and (C) normalized fluorescence intensity of CS-Py$^+$ by continuous irradiation with two-photon NIR pulsed laser (900 nm, output intensity of 2476 mW) at different scans. The image was scanned about every 5.2 s. Scale bar: 20 μm.

that in DMSO (Fig. 2D), probably because of the formation of loosely packed aggregates. In addition, the existence of aggregates in water solution with 5% DMSO were confirmed by dynamic light scattering data with hydrated diameters of 148 and 156 nm for CS-Py$^+$SO$_3^-$ and CS-Py$^+$, respectively (Fig. 2E). The solid FL of CS-Py$^+$SO$_3^-$ and CS-Py$^+$ displayed NIR emissions of 679 nm and 685 nm for CS-Py$^+$SO$_3^-$ and CS-Py$^+$, respectively (Fig. 2F). The absolute FL quantum yields of CS-Py$^+$SO$_3^-$ and CS-Py$^+$ were measured to be 12.8% and 13.7%, respectively, which were advantageous for bioimaging especially for *in vivo* imaging. The maximal emission wavelengths of CS-Py$^+$SO$_3^-$ and CS-Py$^+$ basically increased from toluene, THF, acetone, MeOH to DMSO (Fig. S15), indicating the phenomenon of positive solvatochromism. However, the fluorescence intensity of CS-Py$^+$SO$_3^-$ and CS-Py$^+$ greatly decreased in high polar solvent compared with that in low polar solvent (Fig. 2G and H), due to their TICT property. These data demonstrated that CS-Py$^+$SO$_3^-$ and CS-Py$^+$ are typical donor-acceptor molecules. Furthermore, the two-photon excited fluorescence of CS-Py$^+$SO$_3^-$ and CS-Py$^+$ was investigated in THF using a femtosecond pulsed laser as excitation source (800–980 nm). The data in Fig. S16 clearly revealed that CS-Py$^+$SO$_3^-$ and CS-Py$^+$ showed good two-photon absorption. Using rhodamine in MeOH as the standard [64], the two-photon absorption cross sections of these AIEgens were calculated at different excitation wavelengths (Fig. 2I). CS-Py$^+$SO$_3^-$ and CS-Py$^+$ exhibit good two-photon absorption cross sections (about 30–88 GM at 860–900 nm), which were comparable with those of the standard rhodamine B [64].

3.3. In vitro cell imaging

Before evaluating the biological imaging application, we first investigated the cytotoxicity of CS-Py$^+$SO$_3^-$ and CS-Py$^+$ by standard MTT (3-(4,5-Dimethyl-2-thiazolyl)-2,5-diphenyl-2*H*-tetrazolium bromide) assay. After incubation in HeLa cells for 24 h, the cell viabilities of CS-Py$^+$SO$_3^-$ and CS-Py$^+$ were basically over 85% (Fig. 3). CS-Py$^+$SO$_3^-$ and CS-Py$^+$ exhibited negligible cytotoxicity within the concentration range texted and a low concentration of 1 μM was used in the following imaging experiments.

To demonstrate their biological applications, we performed fluorescence imaging in live HeLa cells by confocal laser scanning microscopy. After incubation for 20 min, bright fluorescence of CS-Py$^+$SO$_3^-$ and CS-Py$^+$ in HeLa cells could be obtained (Fig. S17), indicating their excellent cell staining property. It should be noted that AIEgen CS-Py$^+$SO$_3^-$ probably stained cell membrane, while CS-Py$^+$ stained subcellular organelle in the cytoplasm. *In situ* fluorescence spectra of AIEgen CS-Py$^+$SO$_3^-$ and CS-Py$^+$ in HeLa cells were acquired by using the Lambda mode (Fig. S18). The *in situ* fluorescence data of CS-Py$^+$SO$_3^-$ and CS-Py$^+$ in live cells showed blue-shift feature compared with that in THF, probably due to their TICT effect [65]. Considering their AIE property and TICT effect, we anticipated that CS-Py$^+$SO$_3^-$ and CS-Py$^+$ showed very faint emission at low incubation concentration (1 μM) due to the molecular motion, but they could boosted their blue-shifted emission in low polar (TICT effect) and restricted viscous environment in live cells [66], resulting in “wash-free” imaging property. The fluorescence experiments (Fig. S19) as a function of the solvent viscosity by using glycerol as viscous solvent [67] demonstrated the enhanced emissions of CS-Py$^+$SO$_3^-$ and CS-Py$^+$ in restricted viscous environment.

Then we conducted co-staining imaging experiments to confirm the location of CS-Py$^+$SO$_3^-$ and CS-Py$^+$ in live HeLa cells. As predicted, CS-Py$^+$SO$_3^-$ showed good overlap (Pearson's coefficient of 0.82) with commercial membrane dye DiI (Fig. 4A), indicating CS-Py$^+$SO$_3^-$ mainly stains cell membrane. Normally, positive-charged dyes mainly stain mitochondria due to the high negative membrane potential of mitochondria [68,69]. Hence, we found that CS-Py$^+$ very similar distributions in HeLa cells with commercial mitochondria dye MitoTracker Deep Red FM (MTDR) (Fig. 4B), and the corresponding Pearson's coefficient was 0.84, which revealed that AIEgen CS-Py$^+$ is mainly located in mitochondria.

It remains unclear that what mode AIEgens adopt to locate in the live cells. Based on restriction of intramolecular motion (RIM), there are two main modes for AIEgens to boost their emissions: aggregate state and single molecular state in restrict environment. To date, it's still difficult to evaluate the specific mode of an AIEgen inside the organelle. We anticipated that environment-sensitive probes could probably provide some information. It's known that AIEgens with TICT effect show polarity responsive fluorescence [24]. Therefore, TICT-based AIEgens showing specific emission could adopt specific mode of location in live samples. Given their TICT effect, *in situ* blue-shifted fluorescence data, low incubation concentration as well as their staining in membrane-enclosed restricted viscous organelles (cell membrane and mitochondria) [66], the environment-sensitive AIEgen CS-Py$^+$SO$_3^-$ and CS-Py$^+$ probably exist in specific organelles in the form of single molecular state.

3.4. Ex vivo tissue imaging

Impressed by the excellent penetrability and specific organelle location in live cells, we further investigated whether these AIEgens could show specific imaging in live tissues. To demonstrate this, we carried out *ex vivo* imaging in live rat skeletal muscle tissues using CS-Py$^+$ as an example. Fluorescence imaging data indicated that mitochondria are regularly arranged and formed reticulum in muscle with high signal-to-noise ratio (Fig. 5A), while the tubular morphology could be shown in the transverse plane. Such observation is in good agreement with previous data in skeletal muscle tissues obtained by scanning electron microscope (SEM) [62,63,70]. Additionally, co-staining imaging experiments with commercial mitochondria dye MTDR were carried out to confirm the location in live tissues. As shown in Fig. 5B, the staining pattern of CS-Py$^+$ shows a good overlap with that of MTDR and the corresponding Pearson's coefficient is 0.84, further demonstrating the excellent mitochondrial staining of CS-Py$^+$ in live tissues.

Considering the good two-photon absorption cross-section and high two-photon excited fluorescence of CS-Py$^+$ and its impressive live-tissue staining pattern, then we carried out further imaging experiments to evaluate its two-photon imaging ability. After incubation in live tissues for 1 h, we performed two-photon imaging by using a NIR pulsed laser (900 nm). Bright fluorescence from mitochondrial could be captured and such two-photon excited fluorescence was almost identical to that with one-photon excitation (Fig. 5C), indicating the great potential of CS-Py$^+$ in two-photon fluorescence imaging. Compared with one-photon imaging, two-photon imaging [71–75] shows much better performance especially in deep-tissue imaging [76–79]. To verify this merit, we scanned the fluorescent images at different depths along the *z*-axis. For one-photon imaging, the fluorescent images of regularly arranged mitochondria could be captured with satisfied signal-to-noise ratio at a depth of 50 μm and 3D one-photon fluorescent image was successfully reconstructed (Fig. 6A and B and Movie S1). Such depth is comparable to previous depth in rat skeletal muscle tissue obtained also by one-photon excitation (50.9 μm) [62]. However, two-photon excited fluorescence signals of CS-Py$^+$ in muscle tissue could even be obtained at the depth of about 100 μm (Fig. 6C and Movie S2). Likewise, reconstructed 3D two-photon fluorescent image was also realized (Fig. 6D). Interestingly, such depth obtained by two-photon excitation is deeper than those of our recently reported two-photon probes [63,80]. Taken together, the remarkable *ex vivo* two-photon imaging performance renders CS-Py$^+$ as an excellent candidate probe for biomedical imaging of mitochondria in live deep tissues.

Supplementary data related to this article can be found at https://doi.org/10.1016/j.biomaterials.2019.04.002.

3.5. Photostability

The photostability of CS-Py$^+$SO$_3^-$ and CS-Py$^+$ is crucial parameters for their remarkable live cell stain properties. Photostability was first evaluated by continuous irradiation with confocal lasers. As seen in Fig. 7A, the fluorescence intensities of CS-Py$^+$SO$_3^-$ and CS-Py$^+$ showed nominal signal loss after 180 scans, while the fluorescence signals of DiI and MTDR obviously decreased. Given the impressive performance of two-photon fluorescence imaging in live tissues, the photostability of CS-Py$^+$ was further investigated by continuous irradiation with two-photon NIR pulsed laser (900 nm, output intensity of 2476 mW). The fluorescent images were scanned about every 5.2 s. We can see that after scanning for 60 times, the two-photon fluorescent image could be clearly obtained with good signal-to-noise ratio (Fig. 7B). In addition, normalized two-photon fluorescence intensity data in Fig. 7C revealed that CS-Py$^+$ only suffered a low extent of emission drop under exposure to strong two-photon NIR pulsed laser and over 70% of the initial intensity still remained after 60th scan (about 310 s). These data demonstrated that CS-Py$^+$SO$_3^-$ and CS-Py$^+$ exhibit high photobleaching resistance and CS-Py$^+$ can be applied for long-term one-photon and two-photon mitochondrial tracking.

4. Conclusion

In summary, highly photostable cyanostilbene based AIEgens CS-Py$^+$SO$_3^-$ and CS-Py$^+$ with a long alkyl chain substituent and different charge distributions were successfully synthesized. These AIEgens exhibit NIR solid-state emission, large Stokes shift, high fluorescence quantum yield and good two-photon absorption cross section. *In vitro*

imaging data show that CS-Py$^+$SO$_3^-$ and CS-Py$^+$ stain membrane and mitochondria with high biocompatibility in live cells, respectively. By using CS-Py$^+$ as an example, we have realized *ex vivo* two-photon deep-tissue imaging of mitochondria (about 100 μm) in live rat skeletal muscle tissues. Furthermore, these AIEgens especially CS-Py$^+$ exhibit excellent photostability under long-term one-photon and two-photon continuous irradiation. We also have great confidence that these highly photostable two-photon NIR AIEgens with tunable organelle specificity and deep tissue penetration hold much potentials in biomedical applications. This work could further shed light on the development of other photostable bioprobes for two-photon bioimaging and detection in specific organelles in live samples.

Disclosure of conflicts of interest

The authors declare no competing financial interests.

Acknowledgements

This work was partially supported by the National Natural Science Foundation of China (21788102, 51773111, 21490570 and 21490574), the Research Grants Council of Hong Kong (16305015, AoE/P-03/08, AoE/P-02/12, A-HKUST 605/16, C6009-17G and N_HKUST604/14), the Innovation and Technology Commission (ITC-CNERC14SC01 and ITCPD/17-9) and the Science and Technology Plan of Shenzhen (JCYJ20170818113851132, JCYJ20170818113840164, JCYJ201 60229205601482 and JCYJ20180507183832744).

Appendix A. Supplementary data

Supplementary data to this article can be found online at https://doi.org/10.1016/j.biomaterials.2019.04.002.

References

[1] C. Yang, X. Ni, D. Mao, C. Ren, J. Liu, Y. Gao, D. Ding, J. Liu, Seeing the fate and mechanism of stem cells in treatment of ionizing radiation-induced injury using highly near-infrared emissive AIE dots, Biomaterials 188 (2019) 107–117.
[2] M. Collot, T.K. Fam, P. Ashokkumar, O. Faklaris, T. Galli, L. Danglot, A.S. Klymchenko, Ultrabright and fluorogenic probes for multicolor imaging and tracking of lipid droplets in cells and tissues, J. Am. Chem. Soc. 140 (2018) 5401–5411.
[3] G. Niu, P. Zhang, W. Liu, M. Wang, H. Zhang, J. Wu, L. Zhang, P. Wang, Near-infrared probe based on rhodamine derivative for highly sensitive and selective lysosomal pH tracking, Anal. Chem. 89 (2017) 1922–1929.
[4] D. Chen, H. Wang, L. Dong, P. Liu, Y. Zhang, J. Shi, X. Feng, J. Zhi, B. Tong, Y. Dong, The fluorescent bioprobe with aggregation-induced emission features for monitoring to carbon dioxide generation rate in single living cell and early identification of cancer cells, Biomaterials 103 (2016) 67–74.
[5] Q. Yao, H. Li, L. Xian, F. Xu, J. Xia, J. Fan, J. Du, J. Wang, X. Peng, Differentiating RNA from DNA by a molecular fluorescent probe based on the "door-bolt" mechanism biomaterials, Biomaterials 177 (2018) 78–87.
[6] C.M. Ackerman, S. Lee, C.J. Chang, Analytical methods for imaging metals in biology: from transition metal metabolism to transition metal signaling, Anal. Chem. 89 (2017) 22–41.
[7] X. He, L. Li, Y. Fang, W. Shi, X. Li, H. Ma, In vivo imaging of leucine aminopeptidase activity in drug-induced liver injury and liver cancer via a near-infrared fluorescent probe, Chem. Sci. 8 (2017) 3479–3483.
[8] J. Xu, J. Pan, X. Jiang, C. Qin, L. Zeng, H. Zhang, J.F. Zhang, A mitochondria-targeted ratiometric fluorescent probe for rapid, sensitive and specific detection of biological SO2 derivatives in living cells, *Biosens*, Bioelectron 77 (2016) 725–732.
[9] W. Zhang, Y. Wen, D.-X. He, Y.-F. Wang, X.-L. Liu, C. Li, X.-J. Liang, Near-infrared AIEgens as transformers to enhance tumor treatment efficacy with controllable self-assembled redox-responsive carrier-free nanodrug, Biomaterials 193 (2019) 12–21.
[10] H. Cheng, R.-R. Zheng, G.-L. Fan, J.-H. Fan, L.-P. Zhao, X.-Y. Jiang, B. Yang, X.-Y. Yu, S.-Y. Li, X.-Z. Zhang, Mitochondria and plasma membrane dual-targeted chimeric peptide for single-agent synergistic photodynamic therapy, Biomaterials 188 (2019) 1–11.
[11] X. Li, C.y. Kim, J.M. Shin, D. Lee, G. Kim, H.-M. Chung, K.-S. Hong, J. Yoon, Mesenchymal stem cell-driven activatable photosensitizers for precision photodynamic oncotherapy, Biomaterials 187 (2018) 18–26.
[12] W. Wang, G. Liang, W. Zhang, D. Xing, X. Hu, Cascade-promoted photo-chemotherapy against resistant cancers by enzyme-responsive polyprodrug nanoplatforms, Chem. Mater. 30 (2018) 3486–3498.
[13] H. Wang, Y. Chao, J. Liu, W. Zhu, G. Wang, L. Xu, Z. Liu, Photosensitizer-crosslinked in-situ polymerization on catalase for tumor hypoxia modulation & enhanced photodynamic therapy, Biomaterials 181 (2018) 310–317.
[14] Y. Yuan, B. Liu, Visualization of drug delivery processes using AIEgens, Chem. Sci. 8 (2017) 2537–2546.
[15] Z. Yang, A. Sharma, J. Qi, X. Peng, D.Y. Lee, R. Hu, D. Lin, J. Qu, J.S. Kim, Super-resolution fluorescent materials: an insight into design and bioimaging applications, Chem. Soc. Rev. 45 (2016) 4651–4667.
[16] H. Zhu, J. Fan, J. Du, X. Peng, Fluorescent probes for sensing and imaging within specific cellular organelles, Acc. Chem. Res. 49 (2016) 2115–2126.
[17] A.S. Klymchenko, Solvatochromic and fluorogenic dyes as environment-sensitive probes: design and biological applications, Acc. Chem. Res. 50 (2017) 366–375.
[18] C. Wang, Z. Wang, T. Zhao, Y. Li, G. Huang, B.D. Sumer, J. Gao, Optical molecular imaging for tumor detection and image-guided surgery, Biomaterials 157 (2018) 62–75.
[19] X. Zhang, C. Wang, L. Jin, Z. Han, Y. Xiao, Photostable bipolar fluorescent probe for video tracking plasma membranes related cellular processes, ACS Appl. Mater. Interfaces 6 (2014) 12372–12379.
[20] T. Ren, W. Xu, F. Jin, D. Cheng, L. Zhang, L. Yuan, X. Zhang, Rational engineering of bioinspired anthocyanidin fluorophores with excellent two-photon properties for sensing and imaging, Anal. Chem. 89 (2017) 11427–11434.
[21] A. Gandioso, R. Bresolí-Obach, A. Nin-Hill, M. Bosch, M. Palau, A. Galindo, S. Contreras, A. Rovira, C. Rovira, S. Nonell, V. Marchán, Redesigning the coumarin scaffold into small bright fluorophores with far-red to near-infrared emission and large Stokes shifts useful for cell imaging, J. Org. Chem. 83 (2018) 1185–1195.
[22] J. Mei, N.L.C. Leung, R.T.K. Kwok, J.W.Y. Lam, B.Z. Tang, Aggregation-induced emission: together we shine, united we soar!, Chem. Rev. 115 (2015) 11718–11940.
[23] J. Luo, Z. Xie, J.W.Y. Lam, L. Cheng, H. Chen, C. Qiu, H.S. Kwok, X. Zhan, Y. Liu, D. Zhu, B.Z. Tang, Aggregation-induced emission of 1-methyl-1,2,3,4,5-pentaphenylsilole, Chem. Commun. (2001) 1740–1741.
[24] K. Li, Y. Liu, Y. Li, Q. Feng, H. Hou, B.Z. Tang, 2,5-bis(4-alkoxycarbonylphenyl)-1,4-diaryl-1,4-dihydropyrrolo[3,2-b]pyrrole (AAPP) AIEgens: tunable RIR and TICT characteristics and their multifunctional applications, Chem. Sci. 8 (2017) 7258–7267.
[25] J. Wang, X. Gu, P. Zhang, X. Huang, X. Zheng, M. Chen, H. Feng, R.T.K. Kwok, J.W.Y. Lam, B.Z. Tang, Ionization and Anion−π+ interaction: a new strategy for structural design of aggregation-induced emission luminogens, J. Am. Chem. Soc. 139 (2017) 16974–16979.
[26] K. Li, Q. Feng, G. Niu, W. Zhang, Y. Li, M. Kang, K. Xu, J. He, H. Hou, B.Z. Tang, Benzothiazole-based AIEgen with tunable excited-state intramolecular proton transfer and restricted intramolecular rotation processes for highly sensitive physiological pH sensing, ACS Sens. 3 (2018) 920–928.
[27] X. He, Z. Zhao, L.-H. Xiong, P.F. Gao, C. Peng, R.S. Li, Y. Xiong, Z. Li, H.H.Y. Sung, I.D. Williams, R.T.K. Kwok, J.W.Y. Lam, C.Z. Huang, N. Ma, B.Z. Tang, Redox-active AIEgen-derived plasmonic and fluorescent Core@Shell nanoparticles for multimodality bioimaging, J. Am. Chem. Soc. 140 (2018) 6904–6911.
[28] R. Hu, F. Zhou, T. Zhou, J. Shen, Z. Wang, Z. Zhao, A. Qin, B.Z. Tang, Specific discrimination of gram-positive bacteria and direct visualization of its infection towards mammalian cells by a DPAN-based AIEgen, Biomaterials 187 (2018) 47–54.
[29] X. Wang, J. Dai, X. Min, Z. Yu, Y. Cheng, K. Huang, J. Yang, X. Yi, X. Lou, F. Xia, DNA-conjugated amphiphilic aggregation-induced emission probe for cancer tissue imaging and prognosis analysis, Anal. Chem. 90 (2018) 8162–8169.
[30] Y. Cheng, J. Dai, C. Sun, R. Liu, T. Zhai, X. Lou, F. Xia, An intracellular H2O2-responsive AIEgen for the peroxidase-mediated selective imaging and inhibition of inflammatory cells, Angew. Chem. Int. Ed. 57 (2018) 3123–3127.
[31] Y. Cheng, C. Sun, R. Liu, J. Yang, J. Dai, T. Zhai, X. Lou, F. Xia, A multifunctional peptide-conjugated AIEgen for efficient and sequential targeted gene delivery into the nucleus, Angew. Chem. Int. Ed. 58 (2019) 5049–5053.
[32] X. Ni, X. Zhang, X. Duan, H.-L. Zheng, X.-S. Xue, D. Ding, Near-infrared afterglow luminescent aggregation-induced emission dots with ultrahigh tumor-to-liver signal ratio for promoted image-guided cancer surgery, Nano Lett. 19 (2019) 318–330.
[33] F. Ren, P. Liu, Y. Gao, J. Shi, B. Tong, Z. Cai, Y. Dong, Real time bioimaging for mitochondria by taking aggregating process of aggregation-induced emission near-Infrared dyes with wash-free staining, Mater. Chem. Front. 3 (2019) 57–63.
[34] X. Lou, Z. Zhao, B.Z. Tang, Organic dots based on AIEgens for two-photon fluorescence bioimaging, Small 12 (2016) 6430–6450.
[35] Y.-F. Wang, T. Zhang, X.-J. Liang, Aggregation-induced emission: lighting up cells, revealing life!, Small 12 (2016) 6451–6477.
[36] X. Gu, R.T.K. Kwok, J.W.Y. Lam, B.Z. Tang, AIEgens for biological process monitoring and disease theranostics, Biomaterials 146 (2017) 115–135.
[37] G. Feng, B. Liu, Aggregation-induced emission (AIE) dots: emerging theranostic nanolights, Acc. Chem. Res. 51 (2018) 1404–1414.
[38] H. Gao, X. Zhang, C. Chen, K. Li, D. Ding, Unity makes strength: how aggregation-induced emission luminogens advance the biomedical field, Adv. Biosys. 2 (2018) 1800074.
[39] J. Qi, C. Chen, D. Ding, B.Z. Tang, Aggregation-induced emission luminogens: union is strength, gathering illuminates healthcare, Adv. Healthc. Mater. 7 (2018) 1800477.
[40] J. Qi, C. Chen, X. Zhang, X. Hu, S. Ji, R.T.K. Kwok, J.W.Y. Lam, D. Ding, B.Z. Tang, Light-driven transformable optical agent with adaptive functions for boosting cancer surgery outcomes, Nat. Commun. 9 (2018) 1848.
[41] F. Wu, X. Wu, Z. Duan, Y. Huang, X. Lou, F. Xia, Biomacromolecule-functionalized AIEgens for advanced biomedical studies, Small 15 (2019) 1804839.
[42] C. Chen, H. Ou, R. Liu, D. Ding, Regulating the photophysical property of organic/polymer optical agents for promoted cancer phototheranostics, Adv. Mater. 31 (2019) 1806331.

[43] D. Li, W. Qin, B. Xu, J. Qian, B.Z. Tang, AIE nanoparticles with high stimulated emission depletion efficiency and photobleaching resistance for long-term super-resolution bioimaging, Adv. Mater. 29 (2017) 1703643.
[44] Z. Guo, S. Park, J. Yoon, I. Shin, Recent progress in the development of near-infrared fluorescent probes for bioimaging applications, Chem. Soc. Rev. 43 (2014) 16–29.
[45] Y. Zhang, Y. Wang, J. Song, J. Qu, B. Li, W. Zhu, W.-Y. Wong, Near-infrared emitting materials via harvesting triplet excitons: molecular design, properties, and application in organic light emitting diodes, Adv. Opt. Mater. 6 (2018) 1800466.
[46] X. Gu, E. Zhao, T. Zhao, M. Kang, C. Gui, J.W.Y. Lam, S. Du, M.M.T. Loy, B.Z. Tang, A mitochondrion-specific photoactivatable fluorescence turn-on AIE-based bioprobe for localization super-resolution microscope, Adv. Mater. 28 (2016) 5064–5071.
[47] J. Qi, C. Sun, D. Li, H. Zhang, W. Yu, A. Zebibula, J.W.Y. Lam, W. Xi, L. Zhu, F. Cai, P. Wei, C. Zhu, R.T.K. Kwok, L.L. Streich, R. Prevedel, J. Qian, B.Z. Tang, Aggregation-induced emission luminogen with near-infrared-II excitation and near-infrared-I emission for ultradeep intravital two-photon microscopy, ACS Nano 12 (2018) 7936–7945.
[48] C. Zhu, R.T.K. Kwok, J.W.Y. Lam, B.Z. Tang, Aggregation-induced emission: a trailblazing journey to the field of biomedicine, ACS Appl. Bio Mater. 1 (2018) 1768–1786.
[49] B.-K. An, S.-K. Kwon, S.-D. Jung, S.Y. Park, Enhanced emission and its switching in fluorescent organic nanoparticles, J. Am. Chem. Soc. 124 (2002) 14410–14415.
[50] L. Zhu, Y. Zhao, Cyanostilbene-based intelligent organic optoelectronic materials, J. Mater. Chem. C 1 (2013) 1059–1065.
[51] M. Martínez-Abadía, R. Giménez, M.B. Ros, Self-Assembled α-cyanostilbenes for advanced functional materials, Adv. Mater. 30 (2018) 1704161.
[52] J. Zhao, Z. Chi, Y. Zhang, Z. Mao, Z. Yang, E. Ubba, Z. Chi, Recent progress in the mechanofluorochromism of cyanoethylene derivatives with aggregation-induced emission, J. Mater. Chem. C 6 (2018) 6327–6353.
[53] N.I. Shank, K.J. Zanotti, F. Lanni, P.B. Berget, B.A. Armitage, Enhanced photostability of genetically encodable fluoromodules based on fluorogenic cyanine dyes and a promiscuous protein partner, J. Am. Chem. Soc. 131 (2009) 12960–12969.
[54] N.I. Shank, H.H. Pham, A.S. Waggoner, B.A. Armitage, Twisted cyanines: a non-planar fluorogenic dye with superior photostability and its use in a protein-based fluoromodule, J. Am. Chem. Soc. 135 (2013) 242–251.
[55] X. Shi, C.Y.Y. Yu, H. Su, R.T.K. Kwok, M. Jiang, Z. He, J.W.Y. Lam, B.Z. Tang, A red-emissive antibody-AIEgen conjugate for turn-on and wash-free imaging of specific cancer cells, Chem. Sci. 8 (2017) 7014–7024.
[56] C.Y.Y. Yu, H. Xu, S. Ji, R.T.K. Kwok, J.W.Y. Lam, X. Li, S. Krishnan, D. Ding, B.Z. Tang, Mitochondrion-anchoring photosensitizer with aggregation-induced emission characteristics synergistically boosts the radiosensitivity of cancer cells to ionizing radiation, Adv. Mater. 29 (2017) 1606167.
[57] G. Niu, R. Zhang, J.P.C. Kwong, J.W.Y. Lam, C. Chen, J. Wang, Y. Chen, X. Feng, R.T.K. Kwok, H.H.Y. Sung, I.D. Williams, M.R.J. Elsegood, J. Qu, C. Ma, K.S. Wong, X. Yu, B.Z. Tang, Specific two-photon imaging of live cellular and deep-tissue lipid droplets by lipophilic AIEgens at ultralow concentration, Chem. Mater. 30 (2018) 4778–4787.
[58] C.-K. Lim, S. Kim, I.C. Kwon, C.-H. Ahn, S.Y. Park, Dye-condensed biopolymeric hybrids: chromophoric aggregation and self-assembly toward fluorescent bionanoparticles for near infrared bioimaging, Chem. Mater. 21 (2009) 5819–5825.
[59] H. Lu, Y. Zheng, X. Zhao, L. Wang, S. Ma, X. Han, B. Xu, W. Tian, H. Gao, Highly efficient far red/near-infrared solid fluorophores: aggregation-induced emission, intramolecular charge transfer, twisted molecular conformation, and bioimaging applications, Angew. Chem. Int. Ed. 55 (2016) 155–159.
[60] L. Guo, R. Zhang, Y. Sun, M. Tian, G. Zhang, R. Feng, X. Li, X. Yu, X. He, Styrylpyridine salts-based red emissive two-photon turn-on probe for imaging the plasma membrane in living cells and tissues, Analyst 141 (2016) 3228–3232.
[61] Y. Ye, Y. Zheng, C. Ji, J. Shen, M. Yin, Self-assembly and disassembly of amphiphilic zwitterionic perylenediimide vesicles for cell membrane imaging, ACS Appl. Mater. Interfaces 9 (2017) 4534–4539.
[62] R. Zhang, Y. Sun, M. Tian, G. Zhang, R. Feng, X. Li, L. Guo, X. Yu, J.Z. Sun, X. He, A phospholipid-biomimetic fluorescent mitochondrial probe with ultrahigh selectivity enables in-situ and high-fidelity tissue imaging, Anal. Chem. 89 (2017) 6575–6582.
[63] R. Zhang, G. Niu, X. Li, L. Guo, H. Zhang, R. Yang, Y. Chen, X. Yu, B.Z. Tang, Reaction-free and MMP-independent fluorescent probes for long-term mitochondria visualization and tracking, Chem. Sci. 10 (2019) 1994–2000.
[64] N.S. Makarov, M. Drobizhev, A. Rebane, Two-photon absorption standards in the 550–1600 nm excitation wavelength range, Opt. Express 16 (2008) 4029–4047.
[65] S. Sasaki, G.P.C. Drummen, G.-i. Konishi, Recent advances in twisted intramolecular charge transfer (TICT) fluorescence and related phenomena in materials chemistry, J. Mater. Chem. C 4 (2016) 2731–2743.
[66] D. Su, C.L. Teoh, L. Wang, X. Liu, Y.-T. Chang, Motion-induced change in emission (MICE) for developing fluorescent probes, Chem. Soc. Rev. 46 (2017) 4833–4844.
[67] M.A. Haidekker, E.A. Theodorakis, Molecular rotors—fluorescent biosensors for viscosity and flow, Org. Biomol. Chem. 5 (2007) 1669–1678.
[68] H. Huang, L. Yang, P. Zhang, K. Qiu, J. Huang, Y. Chen, J. Diao, J. Liu, L. Ji, J. Long, H. Chao, Real-time tracking mitochondrial dynamic remodeling with two-photon phosphorescent iridium (III) complexes, Biomaterials 83 (2016) 321–331.
[69] J. Zielonka, J. Joseph, A. Sikora, M. Hardy, O. Ouari, J. Vasquez-Vivar, G. Cheng, M. Lopez, B. Kalyanaraman, Mitochondria-Targeted triphenylphosphonium-based compounds: syntheses, mechanisms of action, and therapeutic and diagnostic applications, Chem. Rev. 117 (2017) 10043–10120.
[70] B. Glancy, L.M. Hartnell, D. Malide, Z.-X. Yu, C.A. Combs, P.S. Connelly, S. Subramaniam, R.S. Balaban, Mitochondrial reticulum for cellular energy distribution in muscle, Nature 523 (2015) 617.
[71] S. Wang, Z. Li, X. Liu, S. Phan, F. Lv, K.D. Belfield, S. Wang, K.S. Schanze, Two-photon absorption of cationic conjugated polyelectrolytes: effects of aggregation and application to 2-photon-sensitized fluorescence from green fluorescent protein, Chem. Mater. 29 (2017) 3295–3303.
[72] H. Zhang, J. Liu, L. Wang, M. Sun, X. Yan, J. Wang, J.-P. Guo, W. Guo, Amino-Si-rhodamines: a new class of two-photon fluorescent dyes with intrinsic targeting ability for lysosomes, Biomaterials 158 (2018) 10–22.
[73] Y.L. Pak, S.J. Park, D. Wu, B. Cheon, H.M. Kim, J. Bouffard, J. Yoon, N-heterocyclic carbene boranes as reactive oxygen species-responsive materials: application to the two-photon imaging of hypochlorous acid in living cells and tissues, Angew. Chem. Int. Ed. 57 (2018) 1567–1571.
[74] W. Qin, P. Zhang, H. Li, J.W.Y. Lam, Y. Cai, R.T.K. Kwok, J. Qian, W. Zheng, B.Z. Tang, Ultrabright red AIEgens for two-photon vascular imaging with high resolution and deep penetration, Chem. Sci. 9 (2018) 2705–2710.
[75] H. Li, Y. Li, Q. Yao, J. Fan, W. Sun, S. Long, K. Shao, J. Du, J. Wang, X. Peng, In situ imaging of aminopeptidase N activity in hepatocellular carcinoma: a migration model for tumour using an activatable two-photon NIR fluorescent probe, Chem. Sci. 10 (2019) 1619–1625.
[76] M. Pawlicki, H.A. Collins, R.G. Denning, H.L. Anderson, Two-photon absorption and the design of two-photon dyes, Angew. Chem. Int. Ed. 48 (2009) 3244–3266.
[77] L. Guo, M.S. Wong, Multiphoton excited fluorescent materials for frequency up-conversion emission and fluorescent probes, Adv. Mater. 26 (2014) 5400–5428.
[78] H.M. Kim, B.R. Cho, Small-molecule two-photon probes for bioimaging applications, Chem. Rev. 115 (2015) 5014–5055.
[79] L. Qian, L. Li, S.Q. Yao, Two-photon small molecule enzymatic probes, Acc. Chem. Res. 49 (2016) 626–634.
[80] Z. Zheng, T. Zhang, H. Liu, Y. Chen, R.T.K. Kwok, C. Ma, P. Zhang, H.H.Y. Sung, I.D. Williams, J.W.Y. Lam, K.S. Wong, B.Z. Tang, Bright near-infrared aggregation-induced emission luminogens with strong two-photon absorption, excellent organelle specificity, and efficient photodynamic therapy potential, ACS Nano 12 (2018) 8145–8159.